RSC Advances

PAPER

View Article Online
View Journal | View Issue

Cite this: *RSC Adv.*, 2025, **15**, 33549

Highly efficient removal of *o*-nitrophenol by a green $Ag@ZnFe_2O_4/BC$ catalyst *via* Fenton-like oxidation

Abdelazeem S. Eltaweil,*[a] Kristina Samir,[a] Eman M. Abd El-Monaem[b] and Gehan M. El-Subruiti[a]

This investigation focused on engineering a novel sustainable Fenton-like catalyst from lime for the efficient degradation of *o*-NP. The heterogeneous catalyst consisted of Ag NPs and $ZnFe_2O_4$ that were prepared using lime juice, while waste lime peels were pyrolyzed at 500 °C to fabricate BC. The Fenton-like $Ag@ZnFe_2O_4/BC$ catalyst was analyzed using SEM to study its morphology, FTIR to assess its chemical composition, XPS to define its elemental composition, zeta potential analysis to evaluate its surface charge, and XRD to reveal its crystal structure. The experimental findings of the Fenton-like degradation of the *o*-NP compound revealed that the best catalytic parameters were as follows: pH = 3, mass of $Ag@ZnFe_2O_4/BC$ = 0.01 g, concentration of H_2O_2 = 500 mg L^{-1}, temperature = 25 °C, and concentration of *o*-NP = 100 mg L^{-1}. Kinetic assessments showed the suitability of second-order kinetics to model the Fenton-like degradation of *o*-NP by $Ag@ZnFe_2O_4/BC$. The mechanistic study suggested the synergistic effect of adsorption and Fenton-like processes, in which several adsorption pathways dominated *o*-NP adsorption, including pi–pi interactions, electron donor–acceptor interactions, coordination bonds, and hydrogen bonds. The Fenton-like reaction of *o*-NP proceeded *via* the free radical Fenton-like mechanism using the active species of $Ag@ZnFe_2O_4/BC$, comprising Fe^{2+}, Ag^0, and EPFRs-BC for activating H_2O_2 and yielding $^{\bullet}OH$. GC-MS analysis identified the intermediates yielded throughout the degradation of the *o*-NP compound by the Fenton-like $Ag@ZnFe_2O_4/BC$ catalyst.

Received 20th July 2025
Accepted 26th August 2025

DOI: 10.1039/d5ra05235a

rsc.li/rsc-advances

1 Introduction

Indeed, water contamination has become one of the most concerning global issues in recent years. Notably, industrial wastewater is deemed the major source of water contamination, where diverse industries drain high concentrations of hazardous substances such as phenolic compounds. Nitrophenols, such as *o*-nitrophenol (*o*-NP), degrade quickly in water, but they require an extended period to degrade in deep groundwater and soil.[1] Notably, *o*-NP poses extreme danger to animals, plants, marine life, and humans. Nevertheless, *o*-NP is used in everyday life in foams, pesticides, adhesives, glues, fabrics, emulsifiers, laundry detergents, colors, exploding substances, rubber-based materials, and acrylics.[2] Consequently, finding an appropriate method to conquer the concrete hazards of *o*-NP is a research hotspot. Environmental experts have endeavored to develop many wastewater treatment methods, including precipitation, electrochemistry, membranes, treatment with biological agents, adsorption, and Fenton reactions. The Fenton oxidation reaction is one of the best and most successful wastewater treatment procedures for eliminating numerous toxic organic wastes, such as highly volatile phenols, benzene, and benzene derivatives, which are extremely poisonous and barely degradable chemicals.[3]

In 1894, Fenton established the procedure known as the Fenton reaction, which is utilized for purifying wastewater *via* radical oxidation. The Fenton reaction has striking advantages, including non-toxicity, outstanding efficacy, and accessibility (works at ambient temperature and under atmospheric pressure).[4] The homogeneous Fenton process is a simple oxidation reaction between soluble iron ions and hydrogen peroxide (H_2O_2), resulting in reactive oxygen radicals that can attack organic contaminants and degrade them. However, this type of Fenton process has some bottlenecks, such as the poor recyclability of the soluble iron catalyst and a pH of 3–5.[5] On the contrary, the wide pH range operability and eminent reusability of solid catalysts make the heterogeneous Fenton process favorable over the homogeneous process.[6] For this purpose, different types of heterogeneous Fenton catalysts have been ameliorated to boost their catalytic performance, such as metal oxides/ferrites, metal–organic frameworks, carbon-based materials, and layered double hydroxide.[7–9] In particular,

---

[a] Chemistry Department, Faculty of Science, Alexandria University, Alexandria, Egypt. E-mail: abdelazeemeltaweil@alexu.edu.eg; tota.samir96@yahoo.com; gehanmsubruiti@alexu.edu.eg

[b] Advanced Technology Innovation, Borg El-Arab, Alexandria, Egypt. E-mail: emanabdelmonaem2014@gmail.com

green-synthesized catalysts are worthy of attention owing to their eco-benign character to the environment and humans and low energy consumption compared to chemical catalysts, promising catalytic activity, low capital costs, and sustainability.[10]

Silver nanoparticles (Ag NPs) possess exceptional plasmonic, optical, and thermal characteristics, high surface areas, chemical stability, and excellent catalytic activity and stability.[11] These auspicious merits of Ag NPs make them a preeminent catalyst to degrade a variety of organic pollutants, including pharmaceuticals, nitro compounds, and dyes.[12] Interestingly, Ag NPs have exhibited astonishing performance as a Fenton catalyst owing to their high ability to activate H_2O_2 and form hydroxyl radicals ($^{\bullet}OH$).[13] Most of the reported studies on the fabrication of Ag NPs depend on chemical or physical approaches that consume high energy and use harmful reagents. However, the green approach uses naturally reducing agents and has revealed promising results in the morphology, size, chemical stability, and catalytic activity of green-fabricated Ag NPs.[14]

Zinc ferrite ($ZnFe_2O_4$) is a soft ferromagnetic material with a remarkable magnetic character and has gained increasing interest as a catalyst owing to its accessibility, low cost, high surface area, electrical conductivity, superb catalytic activity, mechanical and chemical stability, and surface oxygen mobility.[15] The ferromagnetic nature of $ZnFe_2O_4$ allows its facile, fast, and inexpensive separation from the catalytic media. $ZnFe_2O_4$ NPs are fabricated *via* diverse approaches, including micro-emulsion, co-precipitation, citrate precursor-based, molten salt-based, hydrothermal, and sol–gel methods.[16] However, the green fabrication approach is still the best one from environmental and economic perspectives.

Biochar (BC) is one of the most well-known carbonaceous materials that has attracted significant fame in different sectors, especially wastewater remediation.[17] BC is typically fabricated by the thermal decomposition of biowastes at high temperatures of 300–900 °C. Notably, BC is characterized by its good mechanical properties, ample active oxygenated groups, a porous structure, and a large surface area. The environmentally persistent free radicals (EPFRs) of BC render it a remarkable Fenton-like catalyst because EPFRs can easily activate H_2O_2 and produce high concentrations of $^{\bullet}OH$ radicals.[3]

The heterogeneous Ag NPs, $ZnFe_2O_4$, and BC catalysts have demonstrated superb catalytic activity toward different organic pollutants. For instance, Welter *et al.* prepared $ZnFe_2O_4$-supported BC for decomposing rhodamine B *via* the photo-Fenton reaction. The experimental findings revealed that the photo-Fenton decomposition % of rhodamine B reached 100% within an hour. In addition, the recycling study elucidated the excellent recyclability of $ZnFe_2O_4$@BC for eight runs.[18] In another investigation, Sang and his co-authors studied the catalytic activity of rice straw-derived BC toward the Fenton-like degradation of ciprofloxacin, showing that the decomposition % reached 96.80% within 20 min.[19] Eltaweil *et al.* developed Chenopodium-derived biochar for degrading *o*-NP by fabricating the magnetic Fe_3O_4/MIL-88A/BC catalyst. The degradation % of *o*-NP achieved was 91.04% during 120 min at pH 5 using 10 mg of Fe_3O_4/MIL-88A/BC and 500 mg L^{-1} H_2O_2.[3] In this context, Park *et al.* prepared iron-doped sugarcane BC for decomposing orange *G*, revealing that the Fenton-like decomposition % was 99.70% within 120 min.[8] In another study, Hoang *et al.* synthesized Ag/Ni/Fe_3O_4/AC beads for the photo-Fenton decomposition of enrofloxacin, showing that the degradation % was 96.78%. In addition, the recyclability test demonstrated that the decomposition % of enrofloxacin was 83.61% after reusing the Ag/Ni/Fe_3O_4/AC beads for five runs.[20]

According to previous investigations, Ag NPs and $ZnFe_2O_4$ have not been utilized for decomposing *o*-NP *via* the Fenton-like reaction till now, and there is a shortage of studies that have reported the Fenton-like decomposition of *o*-NP by BC. Consequently, our study highlighted the fabrication of a novel sustainable Fenton-like catalyst from lime for the efficient degradation of *o*-NP. The catalyst was constructed from Ag NPs and $ZnFe_2O_4$, which were synthesized from lime juice, while the remaining lime peels were pyrolyzed at 500 °C to fabricate BC. The chemical, morphological, and magnetic properties of the as-fabricated Ag@$ZnFe_2O_4$/BC were determined using bountiful characterization instruments. The better reaction conditions for the Fenton-like degradation of *o*-NP by Ag@$ZnFe_2O_4$/BC were identified using a series of experiments, comprising the impacts of H_2O_2 concentration, pH medium, system temperature, *o*-NP concentration, and catalyst dose. The degradation mechanism of *o*-NP was studied by scavenging tests and XPS analyses. Furthermore, the intermediate compounds of the *o*-NP degradation reaction were identified by GC-MS. The recyclability of the Ag@$ZnFe_2O_4$/BC catalyst was examined experimentally by cycling tests.

2 Experimental section

The chemicals used, preparation steps and applied characterization instruments are presented in Texts S1 and S2.

2.1 Synthesis of silver nanoparticles

Two or three limes were well-cleaned with distilled water and squeezed to prepare fresh lime juice. The lime juice was filtered through filter paper to remove the lime's dregs. Then, 10 mL of the lime juice was dropped into an aqueous $AgNO_3$ solution (0.01 N, 100 mL). The Ag/lime mixture remained at 30 °C for 24 h under gentle stirring. The resulted Ag NPs were collected, washed, and heated for drying in an oven at 60 °C for 10 h.[5]

2.2 Synthesis of zinc ferrite

$ZnFe_2O_4$ was fabricated by the microwave approach as follows: 100 mL of an aqueous solution of $Zn(NO_3)_2\cdot 6H_2O$ and $Fe(NO_3)_3\cdot 6H_2O$ was stirred for 15 min and labeled as sample A. Next, 5 mL of lime juice (prepared by the same procedure in Section 2.1) was added to 45 mL of distilled H_2O (sample B). Then, samples A and B were mixed under stirring for 30 min and transferred to a microwave oven (2.54 GHz at 900 W) for 15 min. The resultant powder was pyrolyzed for 4 h at 600 °C at a heating rate of 5 °C min^{-1} to form a dark golden-brown powder of $ZnFe_2O_4$.

2.3 Synthesis of biochar

The leftover lime peels from the preparation of Ag NPs and $ZnFe_2O_4$ were cut into small pieces and dried in an oven at 100 °C for 24 h. The dried lime pieces were crushed in a mortar and pestle, converting them to a powder. The lime powder was pyrolyzed for 5 h at 500 °C at a heating rate of 10 °C min^{-1} in an oxygen-free environment, where the crucible was kept in a stainless-steel cylinder and the air in the cylinder was replaced by nitrogen gas. Finally, a dark black fine powder of BC was obtained and stored in a vial.[6]

2.4 Preparation of the composite

The $Ag@ZnFe_2O_4/BC$ catalyst was fabricated by dissolving 0.5 g of $AgNO_3$ in 100 mL of distilled water and then adding 0.1 g of BC and 0.05 g of $ZnFe_2O_4$ to the Ag solution under stirring. After 30 min, 10 mL of fresh lime juice was dropped into the reaction mixture and kept for 24 h at 30 °C. Ultimately, $Ag@ZnFe_2O_4/BC$ was centrifuged, washed, and dried at 60 °C for 10 h.

2.5 Fenton experiment

The Fenton-like degradation process of *o*-NP by $Ag@ZnFe_2O_4/BC$ was optimized as follows: (i) the best pH medium to efficiently degrade the *o*-NP molecules was identified by performing the Fenton-like process in diverse pH media in the range of 3–11. (ii) The favorable catalyst dose was determined by varying the $Ag@ZnFe_2O_4/BC$ dose from 0.005 to 0.02 g. (iii) The suitable H_2O_2 concentration to produce higher $^{\bullet}OH$ proportions was determined by changing the used concentration of H_2O_2 from 100 to 1000 mg L^{-1}. (iv) The influence of raising the catalytic system temperature on the degradation % of *o*-NP was inspected in the temperature range from 25 to 55 °C. (v) The catalytic activity of $Ag@ZnFe_2O_4/BC$ was examined at low and high concentrations of *o*-NP, ranging from 50 to 400 mg L^{-1}. (vi) Finally, the concentration of degraded *o*-NP was investigated by withdrawing a sample after each experiment and measuring it using a spectrophotometer.[21] The degradation efficacy of *o*-NP was defined using eqn (1).

$$\text{Degradation efficiency, DE} = \frac{C_0 - C_t}{C_0} \times 100 \tag{1}$$

3 Results and discussion

3.1 Studying the $Ag@ZnFe_2O_4/BC$ characteristics

3.1.1 XRD. The XRD patterns of Ag, $ZnFe_2O_4$, BC, and $Ag@ZnFe_2O_4/BC$ are depicted in Fig. 1a. The XRD pattern of Ag NPs demonstrated its face-centered cubic structure, with peaks located at the positions of 32.27°, 38.18°, 44.25°, and 64.72°, correlating to the crystallographic planes of (111), (200), (220), and (311), respectively.[22] The XRD pattern of $ZnFe_2O_4$ exhibited diffraction peaks at 2θ positions of 29.92°, 35.28°, 36.92°, 42.88°, 53.16°, 56.72°, and 62.24°, corresponding to the planes of (220), (311), (222), (400), (422), (511), and (440), respectively. These findings confirmed the formation of the cubic structure of the $ZnFe_2O_4$ nanoparticles. The XRD pattern of biochar revealed its concomitant broad peak between $2\theta = 20°$ and 30°, indicating the presence of a stacking structure of aromatic layers. The XRD pattern of the synthesized $Ag@ZnFe_2O_4/BC$ composite showed the diffraction peaks of Ag and $ZnFe_2O_4$ at 2-theta values of 29.92, 35.28, 38.18, 42,88, 44.25, 53.16, 56.72, 62.24, and 64.72, with the lower-intensity ones attributed to the existence of the amorphous BC.

3.1.2 FTIR. The FTIR analysis was employed to analyze the chemical compositions of Ag, $ZnFe_2O_4$, BC, and $Ag@ZnFe_2O_4/BC$, as demonstrated in Fig. 1b. All the analyzed samples showed the peak belonging to OH stretching at around 3400 cm^{-1} and the related peaks to the symmetric and asymmetric C–H stretching at 2923 and 2853 cm^{-1}, respectively.[23] The FTIR spectrum of Ag NPs illustrated their accompanying bands at the wavenumbers of 568 and 532 cm^{-1}, indicating the binding of Ag NPs with oxygen. The FTIR peak at 1733 cm^{-1} and the band near 1647 cm^{-1} were assigned to the C=C stretching (nonconjugated) and –C=O stretching, respectively. Furthermore, the observed peaks in the wavenumber range of 1444–1409 cm^{-1} corresponded to C–H, and the peaks at 1383 and 1072 cm^{-1} were associated with the aromatic ring of the lime and C–O stretching, respectively.[24] The FTIR spectrum of $ZnFe_2O_4$ depicted a peak at 546 cm^{-1}, which coincided with the stretching vibration of tetrahedral metal oxide, while the peaks at 435 and 415 cm^{-1} were associated with the bending vibrations of the metal oxide octahedral site.[25] The peak at 1386 cm^{-1} was attributed to the aromatic ring of the lime; in addition, the peaks at 823 and 624 cm^{-1} were ascribed to C=C and C–H, respectively. The FTIR spectrum of BC showed a peak at 1568 cm^{-1}, which belonged to the stretching vibration of C=C, while the peak at 1426 cm^{-1} corresponded to the C–O stretching vibration. The peaks at 873 and 799 cm^{-1} were related to out-of-plane C–H bending vibration and O–H bending, respectively.[26] The FTIR spectrum of $Ag@ZnFe_2O_4/BC$ illustrated the distinguishing peaks of Ag, $ZnFe_2O_4$, and BC, indicating its successful formation of the composite.

3.1.3 VSM. The magnetic feature is one of the promising specifications of an excellent catalyst because it allows the perfect separation of the catalyst in no time after finishing the catalytic reaction. So, the magnetism of $ZnFe_2O_4$ and $Ag@ZnFe_2O_4/BC$ was measured *via* VSM, as illustrated in Fig. 1c. The hysteresis diagrams of $ZnFe_2O_4$ and $Ag@ZnFe_2O_4/BC$ indicated their soft ferromagnetic properties, where the coercivity magnitudes were 188.98 and 101.56 G, sequentially. Furthermore, the magnetization magnitudes of $ZnFe_2O_4$ and $Ag@ZnFe_2O_4/BC$ were 42.85 and 25.45 emu/g, respectively, denoting their potent magnetic characters. The noticed dwindling in the magnetic character of $ZnFe_2O_4$ after integrating with Ag and BC was because of their non-magnetic properties. At the same time, the magnetization of $Ag@ZnFe_2O_4/BC$ was high enough to be separated by an external magnet.[10]

3.1.4 Zeta potential. The surface charge of the $Ag@ZnFe_2O_4/BC$ composite was recorded using the zeta potential in a wide pH range between 3 and 11, as shown in Fig. 1d. The zeta potential data depicted that the net charges on the $Ag@ZnFe_2O_4/BC$ surface were −6.25, −13.69, −22.15, −36.00, and −39.88 mV when the pH of $Ag@ZnFe_2O_4/BC$ was 3, 5, 7, 9, and 11, respectively. The adsorption process is the initial stage of the

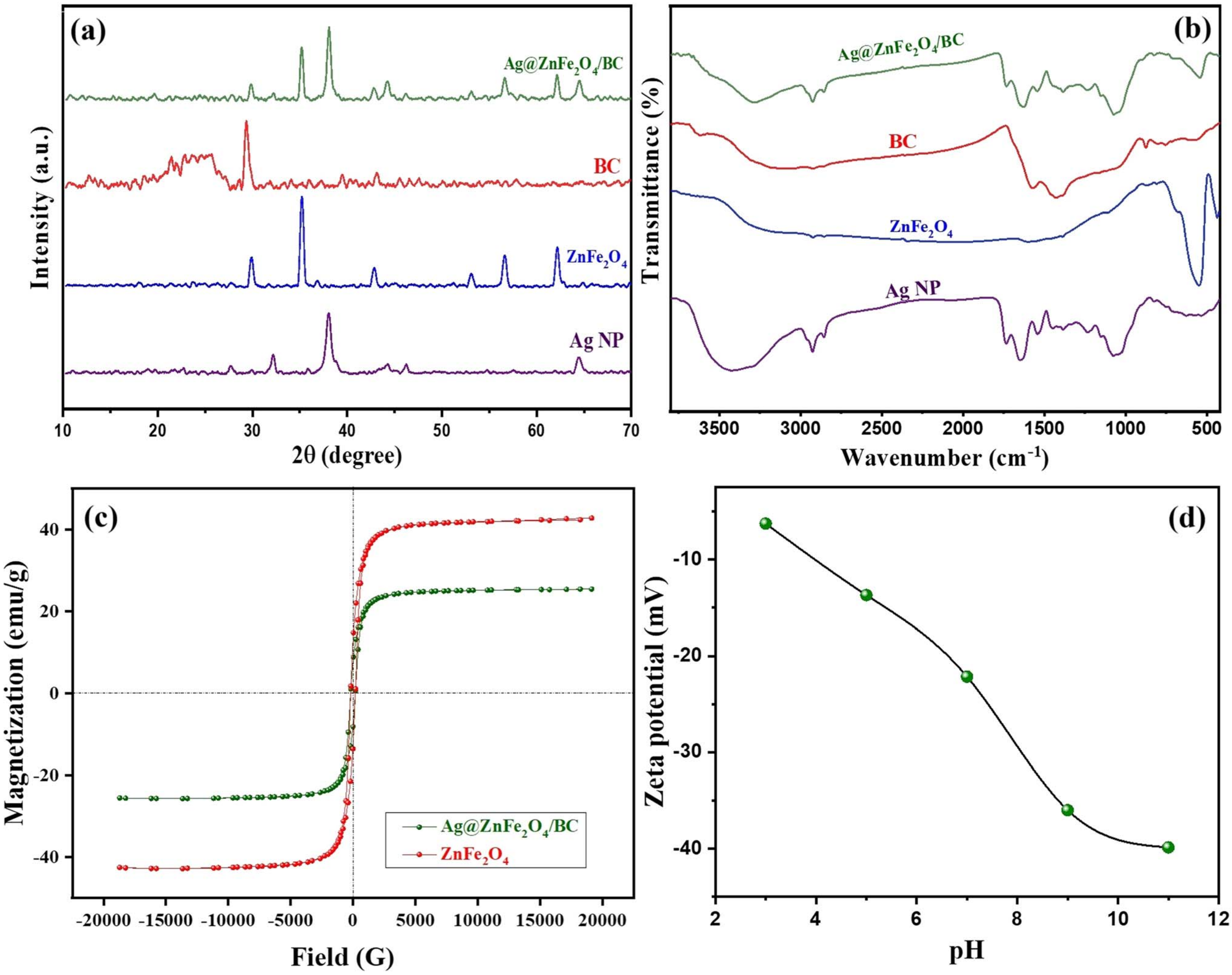

Fig. 1 (a) XRD patterns and (b) FTIR spectra of Ag, $ZnFe_2O_4$, BC, and Ag@$ZnFe_2O_4$/BC. (c) VSM hysteresis loop curves of $ZnFe_2O_4$ and Ag@$ZnFe_2O_4$/BC. (d) Zeta potential curve of Ag@$ZnFe_2O_4$/BC.

catalytic reactions, and usually, electrostatic interactions are the dominant force that controls the adsorption processes. However, the zeta potential results denoted that electrostatic interactions would not be a part of the *o*-NP degradation because *o*-NP exists in the molecular form at pH < 7.23 and in the anionic form at pH > 7.23.

3.1.5 SEM. The SEM analysis revealed a comprehensive understanding of the topological structures of Ag, $ZnFe_2O_4$, BC, and Ag@$ZnFe_2O_4$/BC, as presented in Fig. 2a–d. The SEM image of Ag depicted a unique sheet-like morphology, reflecting the high available surface area of the Ag species. The SEM image of $ZnFe_2O_4$ exhibited adhered particles with a uniform nano-size ranging from 26.15 to 29.60 nm.[27] The SEM image of BC illustrated a highly porous structure with wide pores, confirming the significant role of BC as a good supporter.[28] The SEM image of Ag@$ZnFe_2O_4$/BC confirmed the integration of Ag sheets and $ZnFe_2O_4$ nanoparticles onto the BC surface.

3.1.6 XPS. The XPS analysis was conducted to analyze the elemental composition of the pure Ag@$ZnFe_2O_4$/BC composite (Fig. 3a–f). The survey spectrum confirmed the existence of Ag 3d, Zn 2p, Fe 2p, O 1s, and C 1s at binding energies of 369.06, 1044.5, 714.04, 533.18, and 285.95 eV, respectively. The Ag 3d-XPS spectrum revealed two peaks at 367.93 and 373.86 eV, corresponding to the Ag $3d_{5/2}$ and Ag $3d_{3/2}$ associated with the metallic Ag^0 state, respectively; furthermore, the peaks at 367.35 and 373.66 were assigned to the Ag^+ of Ag $3d_{5/2}$ and Ag $3d_{3/2}$, respectively.[29] The Zn 2p-XPS spectrum depicted peaks at 1022.61 and 1045.53 eV, corresponding to the Zn $2p_{3/2}$ and Zn $2p_{1/2}$ energy levels of Zn^{2+}, respectively.[30] The Fe 2p-XPS spectrum exhibited various peaks at different binding energies, indicating the presence of various oxidation states of iron. The observed peaks at 711.54 and 724.74 eV were attributed to the Fe^{2+} oxidation state, while the manifested peaks at 714.35 and 727.71 eV belonged to the Fe^{3+} oxidation state.[31] The O 1s-XPS spectrum demonstrated peaks at 531.98, 530.28, and 532.28 eV, relating to M–O (M = Ag, Fe, and Zn), M–O–M, and OH, respectively.[32,33] The C 1s-XPS spectrum exhibited peaks at 284.28, 285.38, and 287.28 eV, which were correlated with the C–C/C=C, C–O, and C=O bonds, respectively.[34]

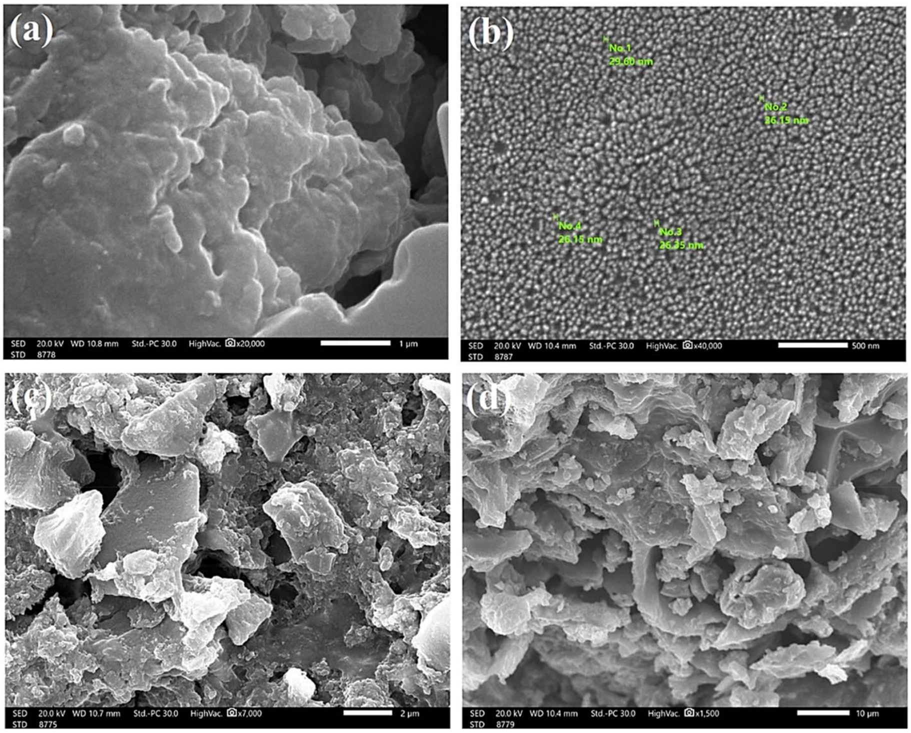

Fig. 2 SEM images of (a) Ag, (b) $ZnFe_2O_4$, (c) BC, and (d) Ag@$ZnFe_2O_4$/BC.

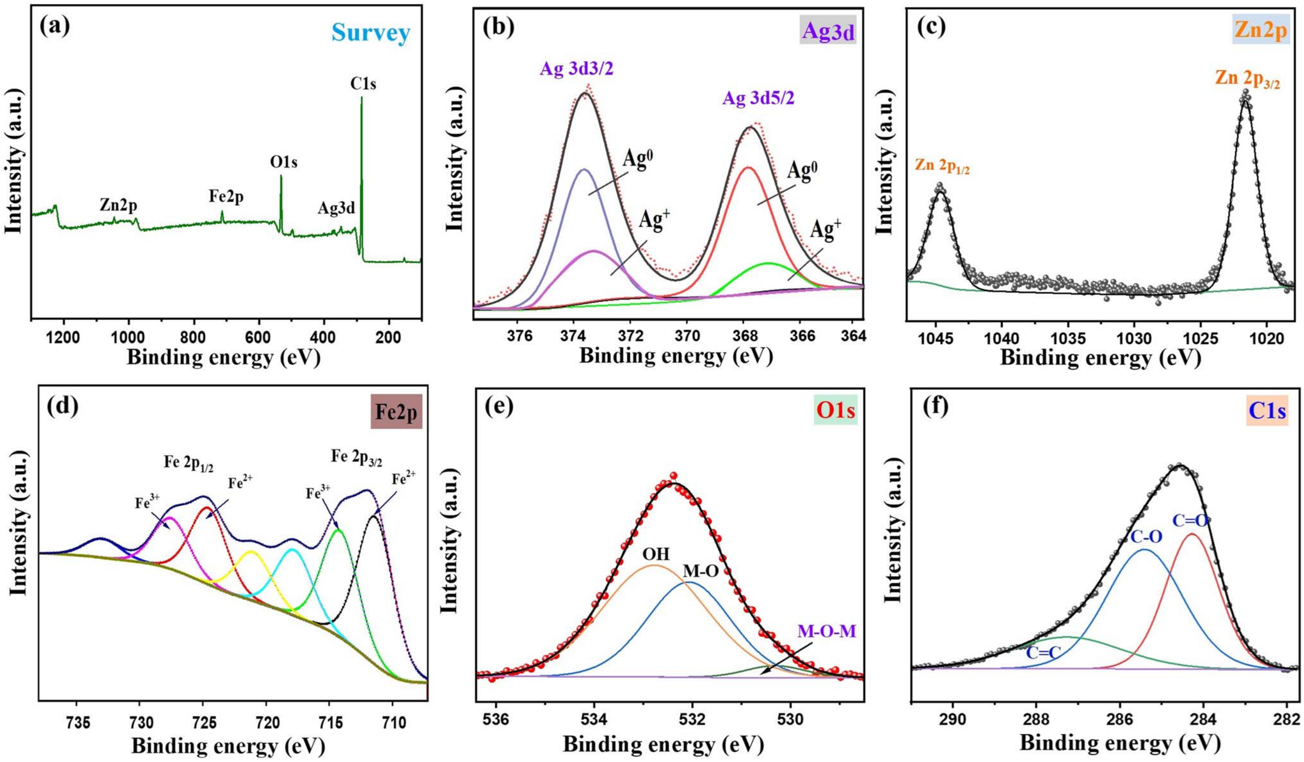

Fig. 3 XPS spectra of the Ag@$ZnFe_2O_4$/BC composite: (a) survey spectrum, (b) Ag 3d, (c) Zn 2p, (d) Fe 2p, (e) O 1s, and (f) C 1s.

3.2 Studying the optimal conditions for *o*-NP degradation

3.2.1 Influence of the catalytic pH medium. The pH of the Fenton-like catalytic degradation medium is a crucial factor that affects the reactivity of the metal ions in the catalysts. The experimental observations revealed that the optimal pH for the Fenton-like reaction of *o*-NP in the Ag@$ZnFe_2O_4$/BC/H_2O_2

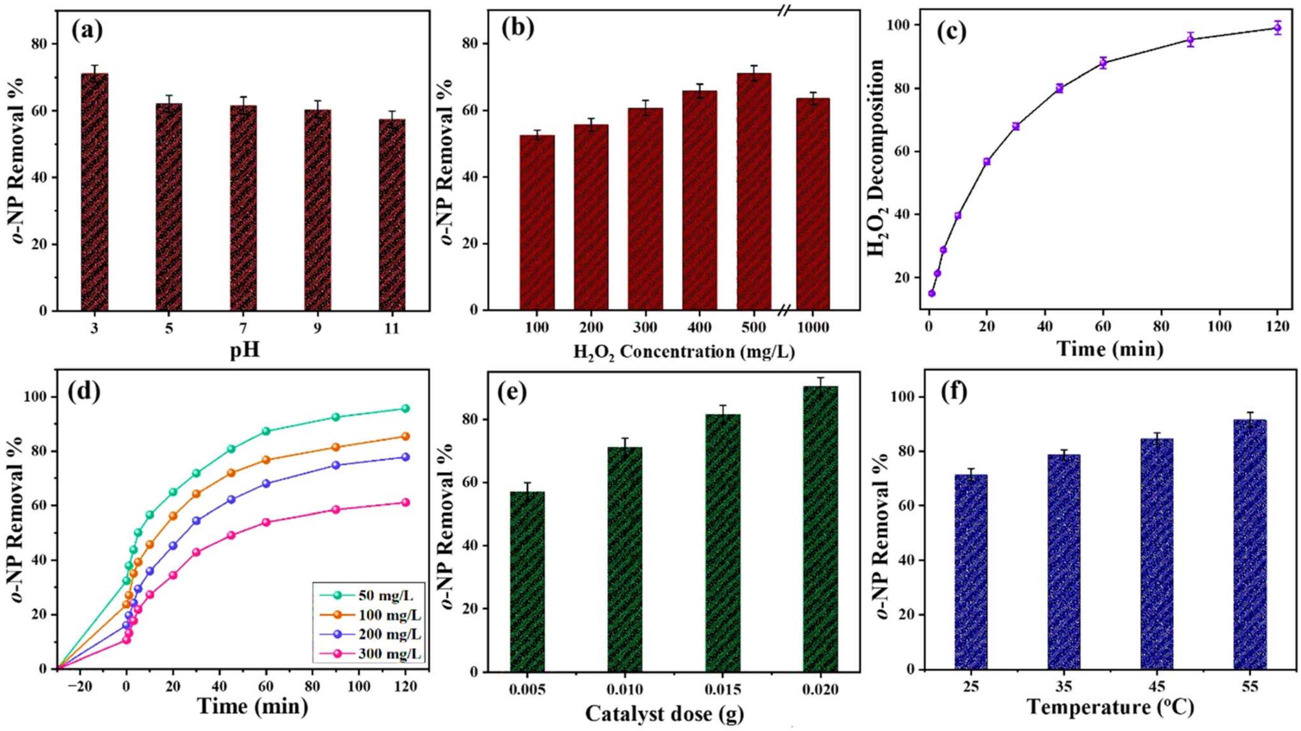

Fig. 4 The experimental findings from the investigation of the catalytic reaction parameters: (a) pH, (b) H_2O_2 concentration, (c) H_2O_2 degradation rate, (d) o-NP concentration, (e) Ag@$ZnFe_2O_4$/BC dosage, and (f) processing temperature.

catalytic system was pH = 3 (Fig. 4a). This result can be explained by the precipitation of the hydroxy iron at near-alkaline pH,[35] at which the iron concentration in the catalytic system decreases, as presented in eqn (2). On the contrary, the H_2O_2 molecules interact with the ample ^{-}OH species in the alkaline medium, creating hydroperoxyl species that tend to attack the metal ions from the catalytic system,[36] as elucidated in eqn (3) and (4). Meanwhile, the H_2O_2 molecules undergo self-decomposition when the pH of the catalytic system becomes more alkaline, diminishing the yield concentration of $^{\bullet}OH$ radicals.[37]

$$Fe^{2+} + {}^{\bullet}OH \rightarrow Fe^{3+} + {}^{-}OH \rightarrow Fe(OH)_3 \tag{2}$$

$$H_2O_2 + {}^{-}OH \rightarrow {}^{-}O_2H + H_2O \tag{3}$$

$$M + {}^{-}O_2H \rightarrow M\ldots{}^{\bullet}O_2H \tag{4}$$

3.2.2 Influence of the initial H_2O_2 concentration. The concentration of H_2O_2 plays a vital role in the concentration of hydroxyl radicals produced during the Fenton degradation reactions. Consequently, the degradation of *o*-NP was tested as a function of the initial H_2O_2 concentration while keeping the pH, temperature, Ag@$ZnFe_2O_4$/BC dosage, and initial *o*-NP concentration constant, as illustrated in Fig. 4b. An increase in the initial concentration of hydrogen peroxide led to a corresponding enhancement in the rate of *o*-NP degradation, with a notable enhancement in the *o*-NP degradation % of 71.14% at a H_2O_2 concentration of 500 mg L^{-1}. This observation can be attributed to the higher yield concentration of $^{\bullet}OH$, boosting the attacked concentration of *o*-NP. However, further increasing the H_2O_2 concentration over 500 mg L^{-1} led to a decrease in the rate of *o*-NP degradation by 7.59%. This deterioration in the degradation % of *o*-NP is attributed to a phenomenon known as self-scavenging because $^{\bullet}OH$ reacts with excess H_2O_2, forming H_2O and $HO_2{}^{\bullet}$, as depicted in eqn (5).

$$H_2O_2 + {}^{\bullet}OH \rightarrow HO_2{}^{\bullet} + H_2O \tag{5}$$

3.2.3 Degradation rate of H_2O_2. The decomposition rate of the H_2O_2 molecules by Ag@$ZnFe_2O_4$/BC was studied in the absence of *o*-NP, as presented in Fig. 4c. The obtained results clarified that the decomposition % of H_2O_2 with 500 mg L^{-1} fulfilled its peak after 120 min, where it was 99.09%. This finding suggests that the *o*-NP degradation reaction will reach equilibrium after 120 minutes, meaning that the H_2O_2 molecules are decomposed completely, and the $^{\bullet}OH$ radicals are almost consumed.[38]

3.2.4 Influence of the initial *o*-NP concentration. The degradation capability of the Fenton-like Ag@$ZnFe_2O_4$/BC catalyst was examined at varying *o*-NP concentrations, ranging from 50 to 300 ppm, as shown in Fig. 4d. The adsorption of *o*-NP with concentrations of 50, 100, 200, and 300 mg L^{-1} was 32.39%, 23.70%, 16.09%, and 10.65%, and the oxidation rates of *o*-NP were 95.65%, 85.43%, 77.83%, and 61.09%, respectively. This diminution in the degradation rate of *o*-NP with its increasing concentration is because of the insufficiency in the

$^{\bullet}$OH yielded compared to the amount of *o*-NP molecules. Furthermore, the high quantities of the *o*-NP molecules in the catalytic medium may block the active functional groups of the Ag@ZnFe$_2$O$_4$/BC catalyst and decrease the produced $^{\bullet}$OH.[39]

3.2.5 Influence of the catalyst dosage. To investigate the ideal Ag@ZnFe$_2$O$_4$/BC dosage to efficiently degrade the *o*-NP molecules, a series of Fenton-like experiments on degrading *o*-NP was conducted at different catalyst masses, as elucidated in Fig. 4e. The results indicated a spontaneous enhancement in the oxidation rate of *o*-NP from 57.05% to 90.46% with the increase in the Ag@ZnFe$_2$O$_4$/BC mass from 0.005 to 0.02 g, sequentially.[40] This observation suggests that increasing the mass of Ag@ZnFe$_2$O$_4$/BC provides a larger number of electrons to activate H$_2$O$_2$, resulting in higher yields of $^{\bullet}$OH.

3.2.6 Influence of the operational temperature. Undoubtedly, the temperature plays a pivotal role in the reactivity of the Fenton-like degradation of *o*-NP by Ag@ZnFe$_2$O$_4$/BC. So, the *o*-NP degradation was studied at different temperatures, starting from room temperature to 55 °C, as demonstrated in Fig. 4f. The degradation rate of *o*-NP ameliorated from 71.34% to 91.56% by raising the operational temperature from 25 to 55 °C. This experimental catalytic performance is attributed to the enhancement in the interaction reactivity between H$_2$O$_2$ and Ag@ZnFe$_2$O$_4$/BC by elevating the reaction temperature, leading to an increased $^{\bullet}$OH concentration and an improved rate of *o*-NP degradation.[41]

3.3 Synergistic effect

To identify the synergistic effect between Ag, ZnFe$_2$O$_4$, and BC to construct a productive Fenton-like catalyst, the *o*-NP degradation was examined by Ag, ZnFe$_2$O$_4$, BC, and Ag@ZnFe$_2$O$_4$/BC (Fig. 5a). In the first step, the adsorption of *o*-NP by Ag, ZnFe$_2$O$_4$, BC, and Ag@ZnFe$_2$O$_4$/BC was 17.29%, 9.31%, 13.29%, and 32.39%, respectively. By contrast, after adding H$_2$O$_2$ in the second step, the Fenton-like degradation percentages of *o*-NP by Ag, ZnFe$_2$O$_4$, BC, and Ag@ZnFe$_2$O$_4$/BC were 49.20%, 33.64%, 39.76%, and 71.85%, respectively.[42] These observations reflect the synergistic effect between Ag, ZnFe$_2$O$_4$, and BC, where their integration results in the formation of a Fenton-like catalyst with a higher degradation aptitude. Furthermore, the results highlight the crucial role of the adsorption process as a prerequisite step that facilitates the subsequent degradation.

3.4 Scavenging effect

To identify the predominant oxygen species in the Fenton-like degradation of *o*-NP by Ag@ZnFe$_2$O$_4$/BC, the catalytic reaction

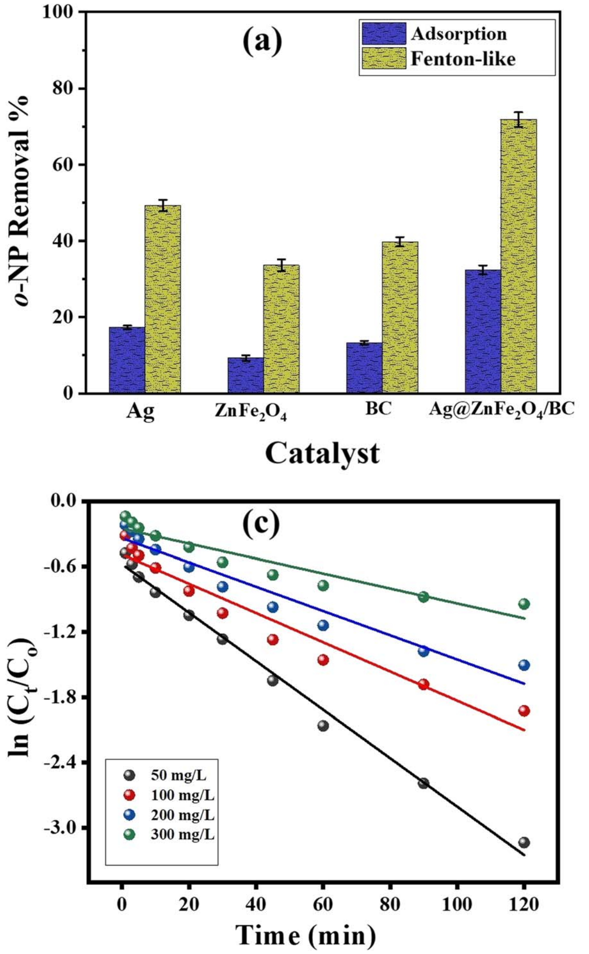

Fig. 5 (a) Synergistic effect test, (b) scavenging test, (c) first-order curve, and (d) second-order curve.

was performed in the existence of scavengers, such as *t*-BuOH and CF (Fig. 5b). Typically, *t*-BuOH can quench the activity of $^{\bullet}OH$ radicals, while CF can hinder $O_2^{\bullet -}$ radicals. The experimental observations clarified a drastic diminution in the degradation percent of *o*-NP in the presence of *t*-BuOH to 27.14%, implying the dominance of $^{\bullet}OH$ in *o*-NP degradation. Contrariwise, the existence of CF in the $H_2O_2/Ag@ZnFe_2O_4/BC$ system did not influence the degradation percent of *o*-NP, indicating that $O_2^{\bullet -}$ is not the predominant oxygen species in the catalytic reaction.[43]

3.5 Kinetics of degradation of *o*-NP

The *o*-NP Fenton-like degradation data for $Ag@ZnFe_2O_4/BC$ within 180 min were inspected by first-order and second-order models (eqn (6) and (7)).

$$\ln \frac{C_t}{C_0} = -k_1 t \tag{6}$$

$$\frac{1}{C_t} = \frac{1}{C_0} + k_2 t \tag{7}$$

where C_t represents the measured *o*-NP concentration at time *t*, C_0 represents the initial *o*-NP concentration, and k_1 and k_2 are the first-order and second-order rate constants, respectively.[44]

The resultant kinetics parameters in Table 1 implied the favorability of the second-order model to represent the Fenton-like degradation of *o*-NP by $Ag@ZnFe_2O_4/BC$, where the R^2 values from the second-order curves at different *o*-NP concentrations are higher than the values of the first-order curves (Fig. 5c and d). In addition, the *o*-NP degradation rate constants were 0.1417, 0.0496, 0.0309, and 0.0134 min^{-1} when the *o*-NP concentrations were 50, 100, 200, and 300 mg L^{-1}, respectively.

Table 1 Parameters from the kinetics study on the Fenton-like degradation of *o*-NP by $Ag@ZnFe_2O_4/BC$

	Concentration (mg L^{-1})			
Kinetic model	50	100	200	300
First order				
k_1	0.0223	0.0.0134	0.0111	0.0069
R^2	0.952	0.945	0.945	0.902
Second order				
k_2	0.1417	0.0496	0.0309	0.0134
R^2	0.990	0.998	0.993	0.950

3.6 Degradation mechanism of the *o*-NP molecules

In light of the experimental finding, the degrading mechanism of *o*-NP occurs *via* two sequential stages. In the first stage, the *o*-NP molecules flow toward the $Ag@ZnFe_2O_4/BC$ surface and adsorb, where the XPS survey of the used catalyst clarified the nitrogen peaks, which confirmed the occurrence of the adsorption process (Fig. 6a). It was supposed that the adsorption step of *o*-NP could occur through various interactions, including (i) the benzene ring of $Ag@ZnFe_2O_4/BC$ could chelate the phenolic ring of *o*-NP through π–π interactions. (ii) The hydroxyl groups (electron donor groups) of $Ag@ZnFe_2O_4/BC$

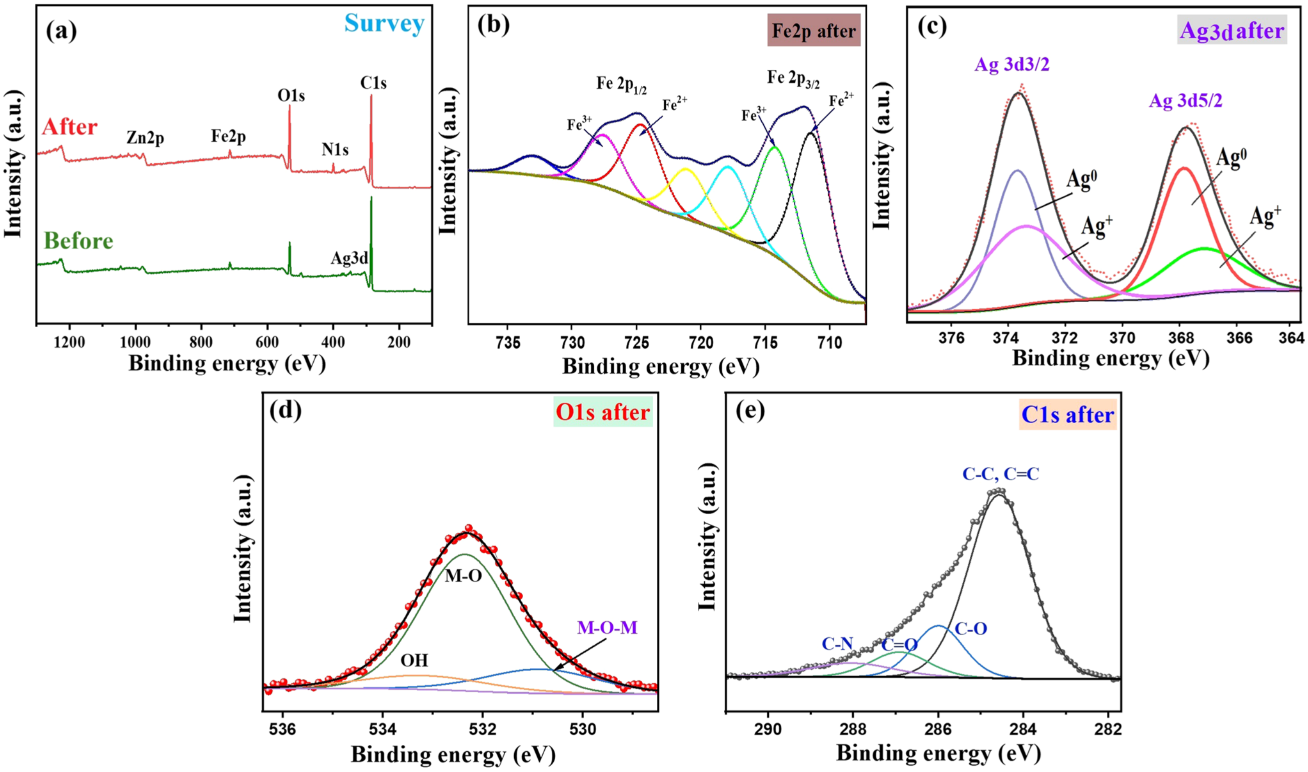

Fig. 6 XPS spectra of the used $Ag@ZnFe_2O_4/BC$ composite: (a) survey spectrum, (b) Fe 2p, (c) Ag 3d, (d) O 1s, and (e) C 1s.

could donate electrons to the nitro group of *o*-NP (electron acceptor groups) *via* electron donor–acceptor interactions. (iii) Coordination bonds could influence the adsorption pathway because Ag@ZnFe$_2$O$_4$/BC contains some transition metal species that could bond to the hydroxyl group of *o*-NP by coordination bonds. (iv) The extra hydrogen in Ag@ZnFe$_2$O$_4$/BC could attach to the oxygen and nitrogen groups of *o*-NP by hydrogen bonds; furthermore, the hydrogen atoms connect to the oxygen species of the composite by hydrogen bonds.[45]

The second stage includes the Fenton-like degradation of the *o*-NP molecules by the Ag@ZnFe$_2$O$_4$/BC catalyst as follows. (i) The Fe^{2+} species, as is well-known, is the cornerstone of the Fenton degradation reaction since it participates in the activation of H$_2$O$_2$ to yield high concentrations of $^{\bullet}$OH radicals, as depicted in eqn (8).[46] As shown in the Fe2p spectrum after the degradation reaction (Fig. 6b), the Fe^{2+} peak shifted from 711.54 and 724.74 eV to 710.54 and 723.84 eV, respectively, and the Fe^{3+} peaks' positions changed from 714.35 and 727.71 eV to 713.08 and 726.86 eV, respectively. Furthermore, the Fe^{3+}/Fe^{2+} ratio in the used Ag@ZnFe$_2$O$_4$/BC increased from 0.705 to 0.788 compared to the pristine catalyst.

(ii) It was deduced in pioneering studies that the Ag^0 species interact with H$_2$O$_2$ in the pH range of 3–4, forming the Ag$^0\cdots$H$_2$O$_2$ complex, as demonstrated in eqn (9).[47] This complex is a short-lived reactive intermediate, and it participates in additional reactions in one pathway to yield the reactive $^{\bullet}$OH radicals, depending on the pH medium, as elucidated in eqn (10).[48] The Ag 3d spectrum of the Ag@ZnFe$_2$O$_4$/BC catalyst after the *o*-NP degradation showed a noticeable increase in the intensity of the peaks belonging to Ag$^+$, along with an increase in the Ag$^+$/Ag^0 ratio from 0.492 to 0.799 (Fig. 6c). This finding indicated the contribution of the Ag^0 species to the Fenton-like degradation of the *o*-NP molecules.

(iii) The EPFR-centered BC in Ag@ZnFe$_2$O$_4$/BC has a significant ability to activate the H$_2$O$_2$ molecules, as clarified in eqn (11), to yield the $^{\bullet}$OH radicals. The O 1s spectrum of Ag@ZnFe$_2$O$_4$/BC after degrading *o*-NP illustrated shifts in the positions of M–O, M–O–M, and OH from 531.98, 530.28, and 532.28 eV to 532.35, 530.84, and 533.20 eV, respectively (Fig. 6d). Additionally, the C–C/C=C, C–O, and C=O peaks shifted from 284.28, 285.38, and 287.28 eV to 284.56, 285.99, and 286.91 eV, respectively, with the appearance of the related peak of C–N at 288.05 eV,[49] as shown in Fig. 6e. Accordingly, the effective contribution of BC in activating H$_2$O$_2$ and producing $^{\bullet}$OH can be deduced. Besides, BC has an additional role that enables it to control half of the redox cycle, where it can recover Fe^{3+} and Ag$^+$ to Fe^{2+} and Ag^0, respectively, as presented in eqn (12) and (13).

Ultimately, the yielded $^{\bullet}$OH radicals from Fe^{2+}, Ag^0, and EPFRs could attack the *o*-NP molecules and degrade them to intermediates that are further degraded to CO$_2$ and H$_2$O (eqn (14)).

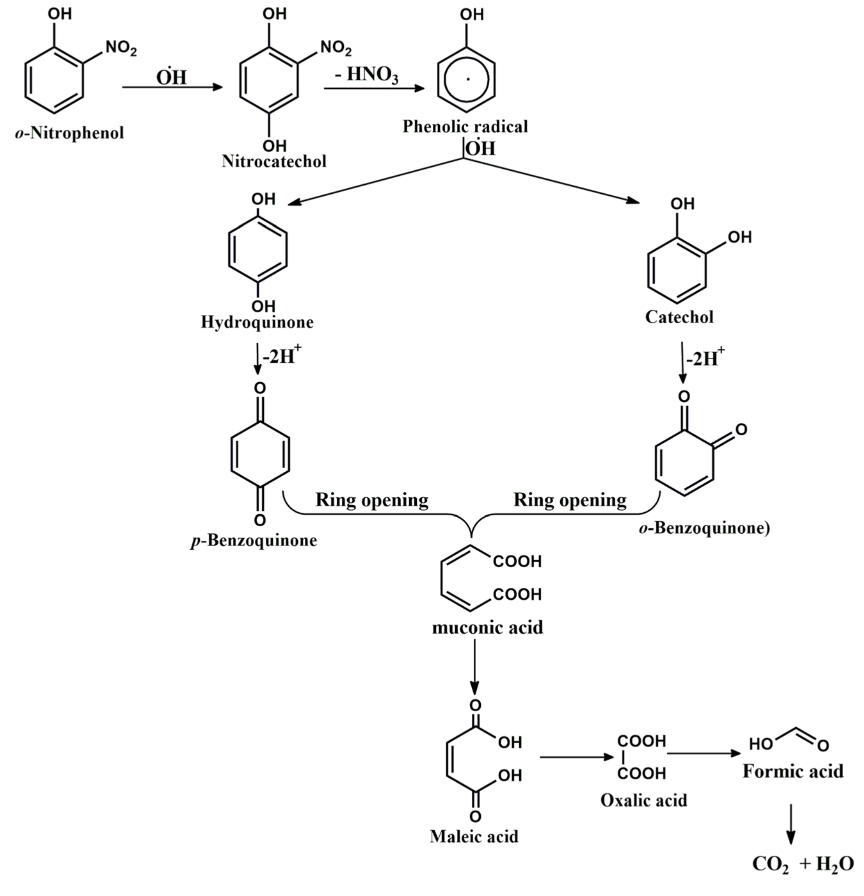

Fig. 7 Schematic of the degradation pathway of *o*-NP by Ag@ZnFe$_2$O$_4$/BC.

$$Fe^{2+} + H_2O_2 \rightarrow Fe^{3+} + {}^{\bullet}OH + {}^{-}OH \tag{8}$$

$$Ag^0 + H_2O_2 \rightarrow Ag^0\cdots H_2O_2 \tag{9}$$

$$Ag^0\cdots H_2O_2 + H^+ \rightarrow Ag^+ + {}^{\bullet}OH + H_2O \tag{10}$$

$$EPFRs + H_2O_2 \rightarrow {}^{\bullet}OH + {}^{-}OH \tag{11}$$

$$Fe^{3+} + \grave{e}_{EPFRs} \rightarrow Fe^{2+} \tag{12}$$

$$Ag^+ + \grave{e}_{EPFRs} \rightarrow Ag^0 \tag{13}$$

$$o\text{-NP} + {}^{\bullet}OH \rightarrow \text{byproducts} \rightarrow CO_2 + H_2O \tag{14}$$

3.7 Degradation pathway of *o*-NP

Based on the GC-MS spectrum (Fig. S1), the *o*-NP molecules were degraded through $^{\bullet}$OH attack, producing nitr*o*-catechol (11.82 min). Then, the $^{\bullet}$OH could hit the adjacent carbon atoms to the nitro group of *o*-NP, forming a phenolic radical (14.94 min). This phenolic radical could be further attacked by $^{\bullet}$OH to produce hydroquinone (23.59 min) and catechol (21.89 min), which were oxidized to *p*-benzoquinone (10.21 min) and *o*-benzoquinone (16.78 min), sequentially. Then, $^{\bullet}$OH could cleave the benzene ring and generate muconic acid (20.56 min) and maleic acid (12.70 min) *via* the ring-opening mechanism, followed by the decomposition of maleic acid to oxalic acid (4.56 min) and then formic acid (7.47 min).[50–53] Fig. 7 depicts a schematic representation of the obtained intermediates throughout the Fenton-like degradation of *o*-NP by Ag@ZnFe$_2$O$_4$/BC.

3.8 Recycling study

A recycling test was conducted for five catalytic runs of *o*-NP degradation by Ag@ZnFe$_2$O$_4$/BC, as shown in Fig. 8. The experimental result revealed the stability of Ag@ZnFe$_2$O$_4$/BC because its catalytic activity toward *o*-NP declined from 94.02% to 84.59% after the fifth cycle. This observation could be attributed to the excellent magnetic properties of Ag@ZnFe$_2$O$_4$/BC, allowing for efficient separation using a magnet and preventing mass loss during the separation process.

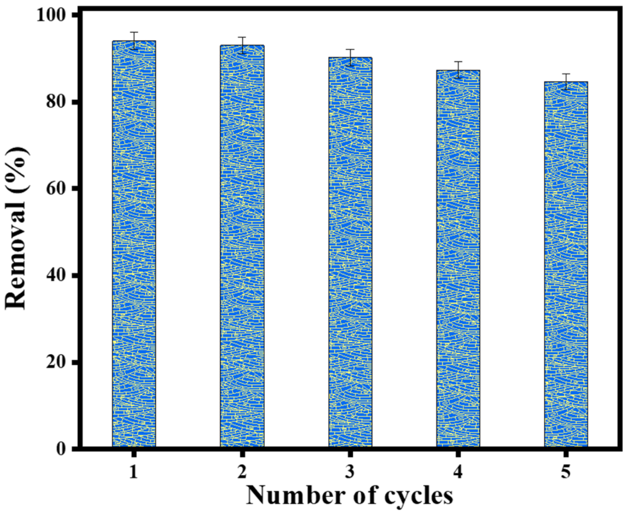

Fig. 8 Recycling study of Ag@ZnFe$_2$O$_4$/BC for five catalytic degradation runs of *o*-NP.

4 Conclusion

In conclusion, the Fenton-like Ag@ZnFe$_2$O$_4$/BC catalyst was green-fabricated using lime to degrade the *o*-NP compound efficiently. The physical and chemical characteristics of Ag@ZnFe$_2$O$_4$/BC were investigated utilizing diverse analysis tools, clarifying that the catalyst's surface carried a negative charge in the pH range from 3 to 11. Moreover, the magnetization magnitude of the ferromagnetic Ag@ZnFe$_2$O$_4$/BC catalyst was about 25.45 emu/g. Notably, the maximal removal % of *o*-NP was 94.02% under the optimal catalytic conditions of pH = 3, mass of Ag@ZnFe$_2$O$_4$/BC = 0.01 g, concentration of H$_2$O$_2$ = 500 mg L^{-1}, temperature = 25 °C, and concentration of *o*-NP = 100 mg L^{-1}. The scavenging test clarified the predominance of $^{\bullet}$OH in the Fenton-like degradation of *o*-NP. Additionally, the free radical degradation mechanism was assessed by XPS analysis, proposing the production of $^{\bullet}$OH by Fe^{2+}, Ag^0, and EPFRs-BC species, with the contribution of EPFRs-BC to recover Fe^{2+} and Ag^0 to form a continuous redox cycle. The recycling test demonstrated that the *o*-NP degradation % was almost equal to 85% after reusing the Ag@ZnFe$_2$O$_4$/BC catalyst for five catalytic runs.

According to the aforementioned findings, the Ag@ZnFe$_2$O$_4$/BC composite is an efficient and reusable heterogeneous catalyst. We provide the following suggestions to inspire readers to develop this work: (i) expand the redox cycle by decorating the catalyst with transition metal-rich substances, like layered double hydroxide. (ii) Shorten the reaction time by introducing more active species to the catalyst, such as MXene and metal–organic frameworks. (iii) Decrease the negative charge on the Ag@ZnFe$_2$O$_4$/BC surface in alkaline media by adding substances with positive net charges, like chitosan, avoiding the hindrance of the electrostatic repulsion forces.

Author contributions

K. S.: methodology, validation, formal analysis, writing – original draft. A. E., E. A.: conceptualization, resources, writing – review & editing, validation, formal analysis, visualization, supervision. G. E.: resources, validation, supervision.

Conflicts of interest

The authors declare no competing interests.

Data availability

The datasets used and analyzed during the current study are available from the corresponding author on reasonable request.

The datasets supporting the findings of this study are available within the article and its SI files. Supplementary information is available. See DOI: https://doi.org/10.1039/d5ra05235a.

Acknowledgements

We want to thank the editor and anonymous reviewers for their valuable comments and suggestions for this paper.

References

1 A. K. Dwivedi, *Int. J. Nat. Sci. Res.*, 2017, **4**, 118–142.
2 S. Zhang, Y. Xu, D. Zhao, W. Chen, H. Li and C. Hou, *Molecules*, 2019, **25**, 124.
3 A. S. Eltaweil, M. S. Ayoup, J. Y. Al Nawah and E. M. Abd El-Monaem, *RSC Adv.*, 2025, **15**, 20111–20124.
4 A. S. Eltaweil, A. M. Galal, E. M. Abd El-Monaem, N. Al Harby and M. E. Batouti, *Nanomaterials*, 2024, **14**, 1282.
5 M. Cheng, W. Song, W. Ma, C. Chen, J. Zhao, J. Lin and H. Zhu, *Appl. Catal., B*, 2008, **77**, 355–363.
6 J. Liao, H. Li, X. Zhang, D. Xiao and N. Qiang, *Appl. Catal., A*, 2015, **491**, 94–99.
7 E. M. Abd El-Monaem, N. Al Harby, M. E. Batouti and A. S. Eltaweil, *Nanomaterials*, 2023, **14**, 54.
8 J.-H. Park, J. J. Wang, R. Xiao, N. Tafti, R. D. DeLaune and D.-C. Seo, *Bioresour. Technol.*, 2018, **249**, 368–376.
9 Z. Yang, X. Tan and C. Zhang, *Sep. Purif. Technol.*, 2024, **336**, 126320.
10 L. Soltys, O. Olkhovyy, T. Tatarchuk and M. Naushad, *Magnetochemistry*, 2021, **7**, 145.
11 A. Meher, A. Tandi, S. Moharana, S. Chakroborty, S. S. Mohapatra, A. Mondal, S. Dey and P. Chandra, *Hyb. Adv.*, 2024, **6**, 100184.
12 S. M. Abbas and K. M. Abas, *BMC Chem.*, 2025, **19**, 221.
13 K. Yang, M. Liu, X. Weng, G. Owens and Z. Chen, *Sep. Purif. Technol.*, 2022, **285**, 120304.
14 E. O. Mikhailova, *Antibiotics*, 2024, **14**, 5.
15 B. Anjaneyulu, Chinmay, V. Chauhan, S. A. Carabineiro and M. Afshari, *J. Inorg. Organomet. Polym. Mater.*, 2024, **34**, 1887–1907.
16 M. Bhattu, R. Acevedo and A. Shnain, 2024.
17 E. M. Abd El-Monaem, A. M. Omer, G. M. El-Subruiti, M. S. Mohy-Eldin and A. S. Eltaweil, *Biomass Convers. Biorefin.*, 2022, 1–13.
18 N. Welter, J. Leichtweis, S. Silvestri, P. I. Z. Sánchez, A. C. C. Mejía and E. Carissimi, *J. Alloys Compd.*, 2022, **901**, 163758.
19 F. Sang, Z. Yin, W. Wang, E. Almatrafi, Y. Wang, B. Zhao, J. Gong, C. Zhou, C. Zhang and G. Zeng, *J. Cleaner Prod.*, 2022, **378**, 134459.
20 V. H. Hoang, T. N. B. Phan, T. T. Le, M. H. Do, V. T. Luu, V. A. Tran, V.-D. Doan and V. T. Le, *RSC Adv.*, 2025, **15**, 13478–13496.
21 A. Babuponnusami and K. Muthukumar, *J. Environ. Chem. Eng.*, 2014, **2**, 557–572.
22 K. Shameli, M. B. Ahmad, A. Zamanian, P. Sangpour, P. Shabanzadeh, Y. Abdollahi and M. Zargar, *Int. J. Nanomed.*, 2012, 5603–5610.
23 P. Khandel, S. Kumar Shahi, L. Kanwar, R. Kumar Yadaw and D. Kumar Soni, *Int. J. Nano Dimens.*, 2018, **9**, 273–285.
24 Q. Ni, T. Zhu, W. Wang, D. Guo, Y. Li, T. Chen and X. Zhang, *Int. J. Mol. Sci.*, 2024, **25**, 1913.
25 A. R. Abbasian and M. Shafiee Afarani, *Appl. Phys. A*, 2019, **125**, 1–12.
26 Y. Liu, X. Zhao, J. Li, D. Ma and R. Han, *Desalin. Water Treat.*, 2012, **46**, 115–123.
27 P. Chen, *J. Sol-Gel Sci. Technol.*, 2017, **82**, 397–406.
28 D. Mohan, K. Abhishek, A. Sarswat, M. Patel, P. Singh and C. U. Pittman, *RSC Adv.*, 2018, **8**, 508–520.
29 A. B. de Paiva, L. M. B. Vargas, M. J. da Silva, A. D. G. Rodrigues, D. A. Soares, M. L. Peres and M. P. F. de Godoy, *Surfaces*, 2022, **5**, 209–217.
30 Y. Zhou, C. Guo, S. Xi, C. Sun, H. Wu and F. Shang, *Res. Chem. Intermed.*, 2017, **43**, 1495–1512.
31 J. Yao, J. Yan, Y. Huang, Y. Li, S. Xiao and J. Xiao, *Front. Chem.*, 2018, **6**, 442.
32 E. M. Abd El-Monaem, M. Hosny and A. S. Eltaweil, *Chem. Eng. Sci.*, 2024, **287**, 119707.
33 A. Stypczyńska, T. Nixon and N. Mason, *Eur. Phys. J. A*, 2014, **68**, 1–10.
34 M. Hosny, M. Fawzy and A. S. Eltaweil, *Sci. Rep.*, 2022, **12**, 7316.
35 R. Deng, H. Luo, D. Huang and C. Zhang, *Chemosphere*, 2020, **255**, 126975.
36 E. M. Abd El-Monaem, J. Y. Al Nawah, M. S. Ayoup and A. S. Eltaweil, *Polymers*, 2025, **17**, 876.
37 A. S. Eltaweil, N. Al Harby, A. I. Osman, M. Alrasheedi, Y. Su and E. M. Abd El-Monaem, *J. Ind. Eng. Chem.*, 2025, **143**, 704–716.
38 A. S. Eltaweil, E. Talaat, E. M. Abd El-Monaem and G. M. El-Subruiti, *J. Solid State Chem.*, 2025, **343**, 125159.
39 R. Selvaraj, V. Nagendran, G. Murugesan, L. C. Goveas, T. Varadavenkatesan, A. Samanth, R. Vinayagam and K. Brindhadevi, *Environ. Res.*, 2024, **250**, 118414.
40 I. Dobrosz-Gómez, J.-D. Quintero-Arias and M.-Á. Gómez-García, *Case Stud. Chem. Environ. Eng.*, 2024, **9**, 100672.
41 B. Zhao, G. Mele, I. Pio, J. Li, L. Palmisano and G. Vasapollo, *J. Hazard. Mater.*, 2010, **176**, 569–574.
42 X. Zhang, B. Bai, G. L. Puma, H. Wang and Y. Suo, *Chem. Eng. J.*, 2016, **284**, 698–707.
43 E. M. Abd El-Monaem, A. M. Omer, A. Heydari, X. k. Ouyang, G. M. El-Subruiti, Y. Xiao and A. S. Eltaweil, *Surf. Interfaces*, 2025, **58**, 105749.
44 Y. Yao, H. Zheng, Z. Tao, Y. Wang, Z. Ma, Y. Qiu and S. Wang, *Appl. Surf. Sci.*, 2023, **613**, 155902.
45 E. M. Abd El-Monaem, A. S. Eltaweil, G. M. El-Subruiti, M. S. Mohy-Eldin and A. M. Omer, *Environ. Sci. Pollut. Res.*, 2023, **30**, 49301–49313.
46 X. Liu, S. Li, Z. Ren, H. Cao, Q. Yang, Z. Luo, L. He, J. Zhao, Q. Wang and G. Li, *Environ. Sci. Technol.*, 2024, **58**, 17797–17806.
47 S. G. Di He and T. D. Waite, *Langmuir*, 2012, **28**, 10266–10275.
48 D. He, A. M. Jones, S. Garg, A. N. Pham and T. D. Waite, *J. Phys. Chem. C*, 2011, **115**, 5461–5468.

49 D. Feng, J. Lü, S. Guo and J. Li, *J. Environ. Chem. Eng.*, 2021, **9**, 104677.

50 J. Qiao, S. Luo, P. Yang, W. Jiao and Y. Liu, *J. Taiwan Inst. Chem. Eng.*, 2019, **99**, 1–8.

51 D. Rajamanickam and M. Shanthi, *Arabian J. Chem.*, 2016, **9**, S1858–S1868.

52 Z. Ye, Y. Zhang, P. Li, L. Yang, R. Zhang and H. Hou, *J. Hazard. Mater.*, 2008, **156**, 356–364.

53 Y. Zhang, K. Zhang, C. Dai, X. Zhou and H. Si, *Chem. Eng. J.*, 2014, **244**, 438–445.